

# Pulsed field magnetization of $0^\circ$ – $0^\circ$ and $45^\circ$ – $45^\circ$ bridge-seeded Y–Ba–Cu–O bulk superconductors

M D Ainslie<sup>1</sup>, J Zou<sup>1</sup>, H Mochizuki<sup>2</sup>, H Fujishiro<sup>2</sup>, Y-H Shi<sup>1</sup>, A R Dennis<sup>1</sup> and D A Cardwell<sup>1</sup>

<sup>1</sup>Bulk Superconductivity Group, Department of Engineering, University of Cambridge, Trumpington Street, Cambridge CB2 1PZ, UK

<sup>2</sup>Department of Materials Science and Engineering, Faculty of Engineering, Iwate University, 4-3-5 Ueda, Morioka 020-8551, Japan

E-mail: [mda36@cam.ac.uk](mailto:mda36@cam.ac.uk)

Received 19 July 2015, revised 6 September 2015

Accepted for publication 19 September 2015

Published 14 October 2015



CrossMark

## Abstract

Large, single-grain (RE)BCO (where RE = rare earth or Y) bulk superconductors with complicated geometries are required for a variety of potential applications, such as rotating machines, magnetic bearings and magnetic separation. As a consequence, the top multi-seeded melt growth process has been studied over many years in an attempt to deliver large, single grains for practical applications. Among these techniques, the so-called bridge-seeding produces the best alignment of two seeds during melt processing of multi-seed samples. In this paper, the trapped field performance and magnetic flux dynamics of two bridge-seeded, multi-seed samples magnetized by pulsed field magnetization are analyzed: one with a  $45^\circ$ – $45^\circ$  and another with a  $0^\circ$ – $0^\circ$  bridge seed. Based on an analysis of the flux penetration across the seeds and in-between the seeds of the  $45^\circ$ – $45^\circ$  multi-seed sample, an estimated  $J_c$  distribution over the  $ab$ -plane is determined, which provides the basis for further analysis via numerical simulation. A three-dimensional finite-element model, developed to qualitatively reproduce and interpret the experimental results, was employed to investigate the influence of the length of the bridge seed for such multi-seed samples. The simulation results agree well with the observed experimental results, in that the multi-seed sample's particular inhomogeneous  $J_c$  distribution acts to distort the trapped field profile from a traditional conical Bean's profile, which is determined by the length and direction of the bridge seed on the bulk surface.

Keywords: bulk superconductors, multi-seeding, bridge-shaped seeds, trapped field magnets, pulsed field magnetization, numerical modelling, finite element method (FEM) modelling

## 1. Introduction

Large, single-grain (RE)BCO (where RE = rare earth element or Yttrium) bulk superconductors have significant potential to trap large magnetic fields over 17 T at temperatures below 30 K [1, 2] and up to 3 T at the technologically important temperature of 77 K [3]. Such materials fabricated into discs and other shapes are potential candidates to replace permanent magnets in applications such as rotating machines [4], magnetic bearings [5–7] and magnetic separation [8].

However, there are several factors that limit the commercial applications of bulk (RE)BCO materials.

Based on the critical state model presented by Bean [9, 10], the peak trapped magnetic field at the centre of disc-shaped bulk superconductor,  $B_{\text{trap}}$ , is given in its simplest form by

$$B_{\text{trap}} = k\mu_0 J_c a, \quad (1)$$

where  $k$  is a geometric constant to account for the sample's finite thickness,  $\mu_0$  is the permeability of free space,  $J_c$  is the

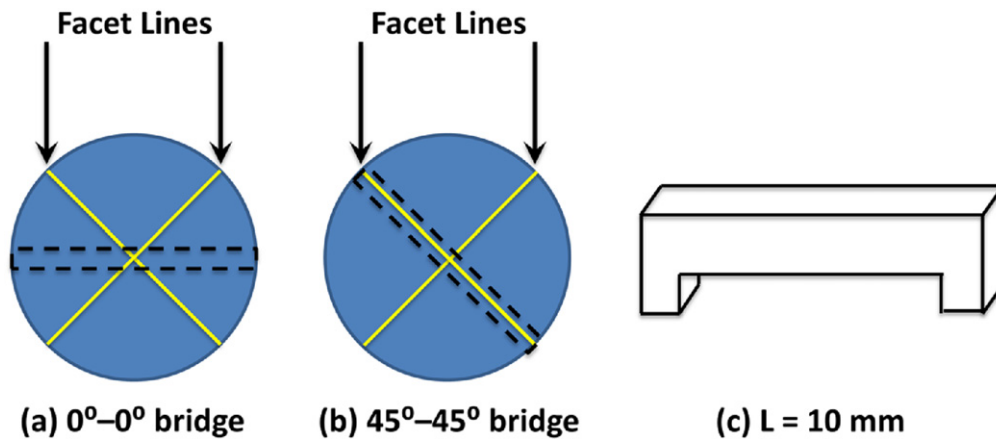


**Figure 1.** Schematic illustration of the single-grain SmBCO samples fabricated by TSMG and the location of (a) the  $0^\circ-0^\circ$  and (b) the  $45^\circ-45^\circ$  bridge-shaped seeds cut subsequently from the parent single grain. (c) An illustration of a bridge-shaped seed.

critical current density and  $a$  is the radius of bulk sample [11]. Therefore, sample size is one of the key factors to improve the trapped field performance of a single-grain sample. Another practical limitation to the fabrication of (RE)BCO samples is their relatively low growth rate; a single-grain bulk sample of diameter around 30 mm takes around one week to complete the growth process. Hence, developing fabrication techniques that reduce the processing time is fundamental to delivering practical, large-scale growth processing.

The multi-seeding process has the potential to enlarge the sample size of (RE)BCO single grains with improved fabrication speed and also provides an opportunity to investigate grain boundaries in bulk samples, which are quite different to those that are formed in thin films and tapes due to the presence of RE-211 components in the bulk material fabricated by top-seeded melt-growth (TSMG). Multi-seeding also allows the development of more complex bulk superconductor shapes, such as bars/rods, rings and cylinders.

Due to these merits, multi-seeding using two or more separate seeds has been investigated over many years [12–18]. However, among the reported studies, poorly-connected grain boundaries form between the two seeds, characterized by a build-up of impurity phases [12–15]. Compared with the trapped field typically generated by single grains, the trapped field in the reported multi-seeded samples have generally been relatively low [16]. In our previous studies on multi-seeding [19–21], a significant improvement was made in the alignment of the seeds in such samples using a novel bridge-seeding technique, which minimizes any misinterpretation of the properties of the multi-seeded sample that may be associated with seed misalignment, rather than with the grain growth itself.

In this paper, the trapped field performance of multi-seeded samples with  $45^\circ-45^\circ$  and  $0^\circ-0^\circ$  aligned bridge seeds magnetized by pulsed field magnetization (PFM) is investigated. The effects of the particular inhomogeneous  $J_c$  distribution on the better-performing  $45^\circ-45^\circ$  multi-seed sample on PFM are modelled numerically using a three-dimensional (3D) finite-element model, developed to qualitatively reproduce and interpret the experimental results. The results agree

qualitatively with the observed experimental results, in that the particular inhomogeneous  $J_c$  distribution of the multi-seed sample acts to influence the magnetic flux dynamics during PFM and distort the trapped field profile, which is determined by the length,  $L$ , and direction of the bridge seed on the bulk surface. This modelling framework will allow further investigation of the influence of different lengths and directions of bridge seeds for such multi-seed samples, to assist in the optimization of the particular setup and characteristics of the PFM process, as well as provide valuable input for the improvement of multi-seed sample processing techniques.

## 2. Bridge-seeded, multi-seed bulk superconductor sample details

### 2.1. Fabrication of the $0^\circ-0^\circ$ and $45^\circ-45^\circ$ bridge-seeds

Due to its higher melting temperature, single-grain Sm–Ba–Cu–O (SmBCO), which forms a suitable seed for the melt processing of YBCO, was fabricated by TSMG using a generic seed [22, 23], from a mixed precursor powder of composition 70 wt% Sm-123 + 30 wt% Sm-211 + 0.1 wt% Pt. The as-grown single grains were cut into slices of length 10 mm parallel to the  $a$  direction of the crystallographic lattice, as shown in figure 1(a), and parallel to a growth facet line on the top surface of the grain, as shown in figure 1(b). These slices were subsequently machined into bridge-shaped seeds, as shown in figure 1(c). The so-called  $45^\circ-45^\circ$  and  $0^\circ-0^\circ$  bridge seeds, labelled according to their relative orientation in the parent grain, were then used to multi-seed the bulk YBCO samples based on controlled alignment and relative orientation of the two legs of the seed [19].

### 2.2. Melt-processing of multi-seed bulk samples using $45^\circ-45^\circ$ and $0^\circ-0^\circ$ bridges

Precursor powders of  $\text{YBa}_2\text{Cu}_3\text{O}_7$  (Y-123),  $\text{Y}_2\text{BaCuO}_5$  (Y-211) and Pt (99% purity) with a starting composition of 70 wt% Y-123 + 30 wt% Y-211 + 0.1 wt% Pt were mixed thoroughly using a motorized mortar and pestle [21]. The

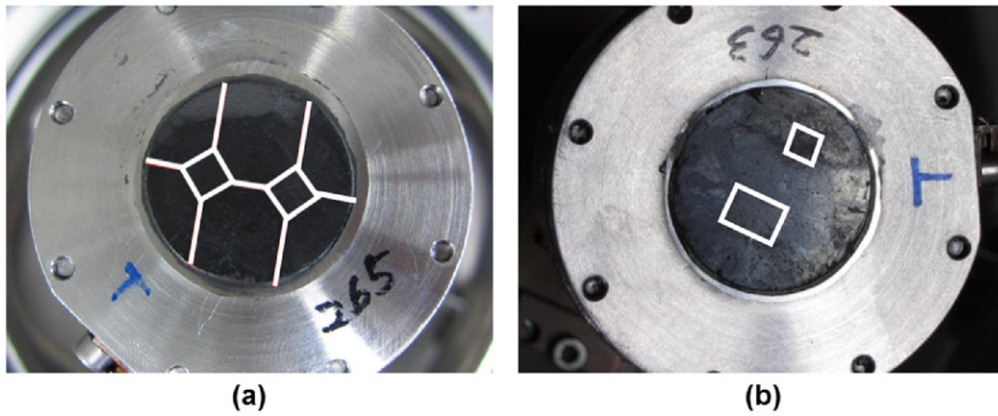


**Figure 2.** Photographs of the bridge-seeded, multi-seed samples under analysis: (a)  $45^\circ\text{--}45^\circ$  orientation, and (b)  $0^\circ\text{--}0^\circ$  orientation. The locations of the seeds (and the growth sector boundaries (GSBs) in the case of the  $45^\circ\text{--}45^\circ$  sample) are shown by the solid white lines.

mixed powder was pressed uniaxially into pellets of diameter 32 mm and thickness 20 mm. Bridge-shaped seeds with a leg separation of 10 mm were placed on the top surface of each pellet. The TSMG technique was used to fabricate the samples, which involves heating each pellet to  $1045^\circ\text{C}$ , holding for 1 h, cooling at  $100^\circ\text{C h}^{-1}$  to  $1005^\circ\text{C}$ , and then cooling more slowly at  $0.4^\circ\text{C h}^{-1}$  to  $970^\circ\text{C}$ . Finally, the samples were furnace-cooled down to room temperature at  $200^\circ\text{C h}^{-1}$ . The multi-seed samples, after machining the bottom surface and polishing, were approximately 25 mm in diameter and 9 mm in height.

Photographs of the  $45^\circ\text{--}45^\circ$  and  $0^\circ\text{--}0^\circ$  bridge-seeded samples are shown in figure 2, and in the case of figure 2(b), it is clear that the seeds in the  $0^\circ\text{--}0^\circ$  configuration have grown differently, resulting in different sizes after polishing. In the following sections, the performance of the samples is analyzed after field cooling (FC) magnetization from around 40 K and PFM at operating temperatures of around 40 K and 65 K.

### 3. Experimental results

#### 3.1. FC magnetization

The FC magnetization technique gives the best indication of the trapped field capability of a bulk superconductor sample. The temperature dependence of the trapped field at the bulk centre is shown in figure 3. FC magnetization was performed with an external field of 7 T at around 40 K. The bulk was heated at a rate of  $0.5\text{ K min}^{-1}$  up to 100 K and the temperature dependence of the trapped field,  $B_z(T)$ , was measured. At around 40 K, the trapped field at the centre of the top surface of the  $45^\circ\text{--}45^\circ$  and  $0^\circ\text{--}0^\circ$  oriented samples is 3.15 T and 1.93 T, respectively, and 1.01 T ( $45^\circ\text{--}45^\circ$ ) and 0.67 T ( $0^\circ\text{--}0^\circ$ ) at 65 K. 2D trapped field distributions at 77 K obtained by FC magnetization are also shown for each sample in figure 4, as measured approximately 1 mm above the top surface using a scanning system consisting of a linear array of Hall probes. It is apparent that the variation in the growth of the seeds in the  $0^\circ\text{--}0^\circ$  oriented sample, in this particular case,

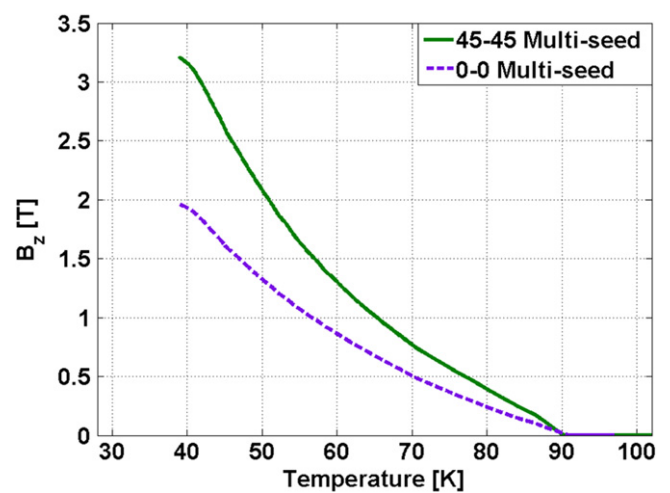


**Figure 3.** Field cooling (FC) magnetization results for the  $45^\circ\text{--}45^\circ$  and  $0^\circ\text{--}0^\circ$  bridge-seeded samples, measured at the centre of the top surface with external applied field around 7 T.

has resulted in a reduced trapped field. This is one of the difficulties in growing such multi-seed samples.

#### 3.2. Pulsed field magnetization

An overview of the PFM experimental setup is described in [24]. The bulk samples were mounted tightly on a sample holder fabricated from 316 stainless steel of inner diameter slightly larger than the diameter of the samples and outer diameter 56 mm to match the dimensions of the available cold stage of the pulse system. Stycast 2850 FT, Catalyst 23 LV was used to mount the samples in the holder, with the epoxy set under vacuum to ensure void-free embedment. The samples were mounted on the cold stage of a Gifford–McMahon, closed cycle helium refrigerator, and a copper magnetizing solenoid pulse coil, cooled using liquid nitrogen, was placed outside the vacuum chamber. The direction of external applied field is parallel to the  $c$ -axis of the bulk samples. The magnetizing coil can provide pulsed external fields up to

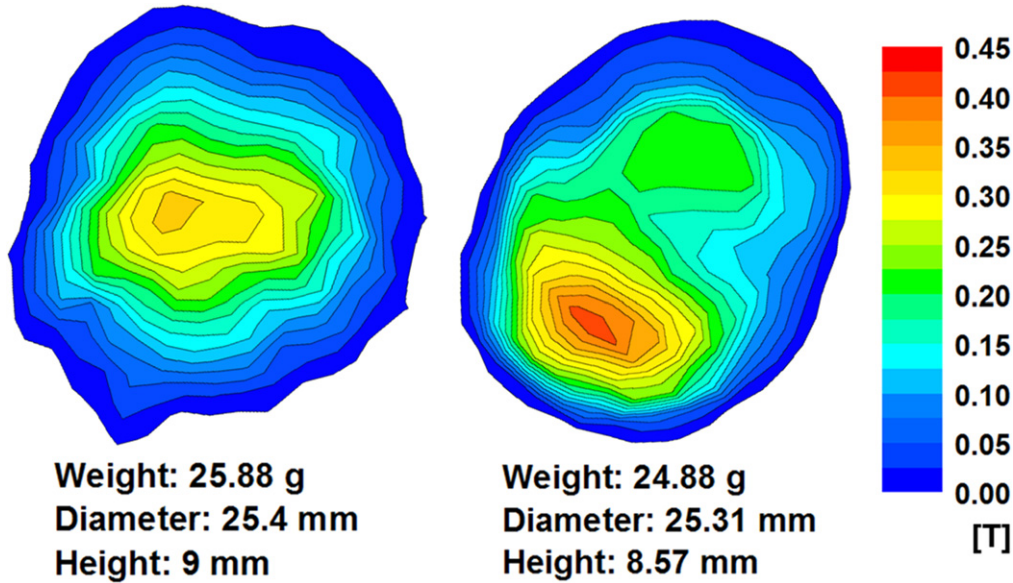


**Figure 4.** Trapped field distributions for each sample, obtained by field cooling (FC) magnetization at 77 K in an external magnetic field of 1.5 T and measured approximately 1 mm above the top surface using a scanning system consisting of a linear array of Hall probes: 45°–45° orientation (left), 0°–0° orientation (right). The samples are aligned in the same position as shown in figure 2.

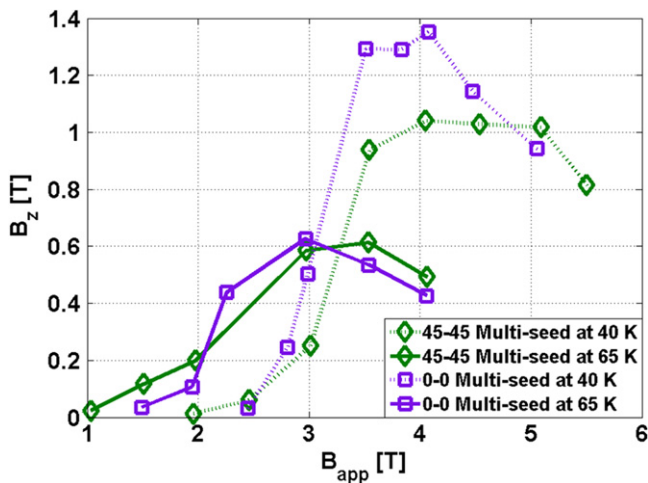


**Figure 5.** Trapped fields for the 45°–45° and 0°–0° samples after PFM at operating temperatures of 40 K and 65 K, measured at the centre of the top bulk surface ( $z = 1$  mm).

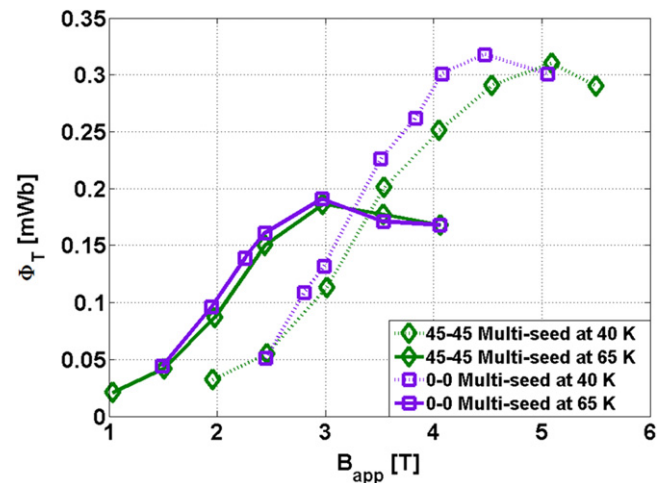


**Figure 6.** Total trapped flux,  $\Phi_T$ , for 45°–45° and 0°–0° samples at operating temperatures of 40 K and 65 K, measured at 1 mm above the bulk surface ( $z = 1$  mm).  $\Phi_T$  is calculated from the 2D trapped field profiles presented in section 3.2.2.

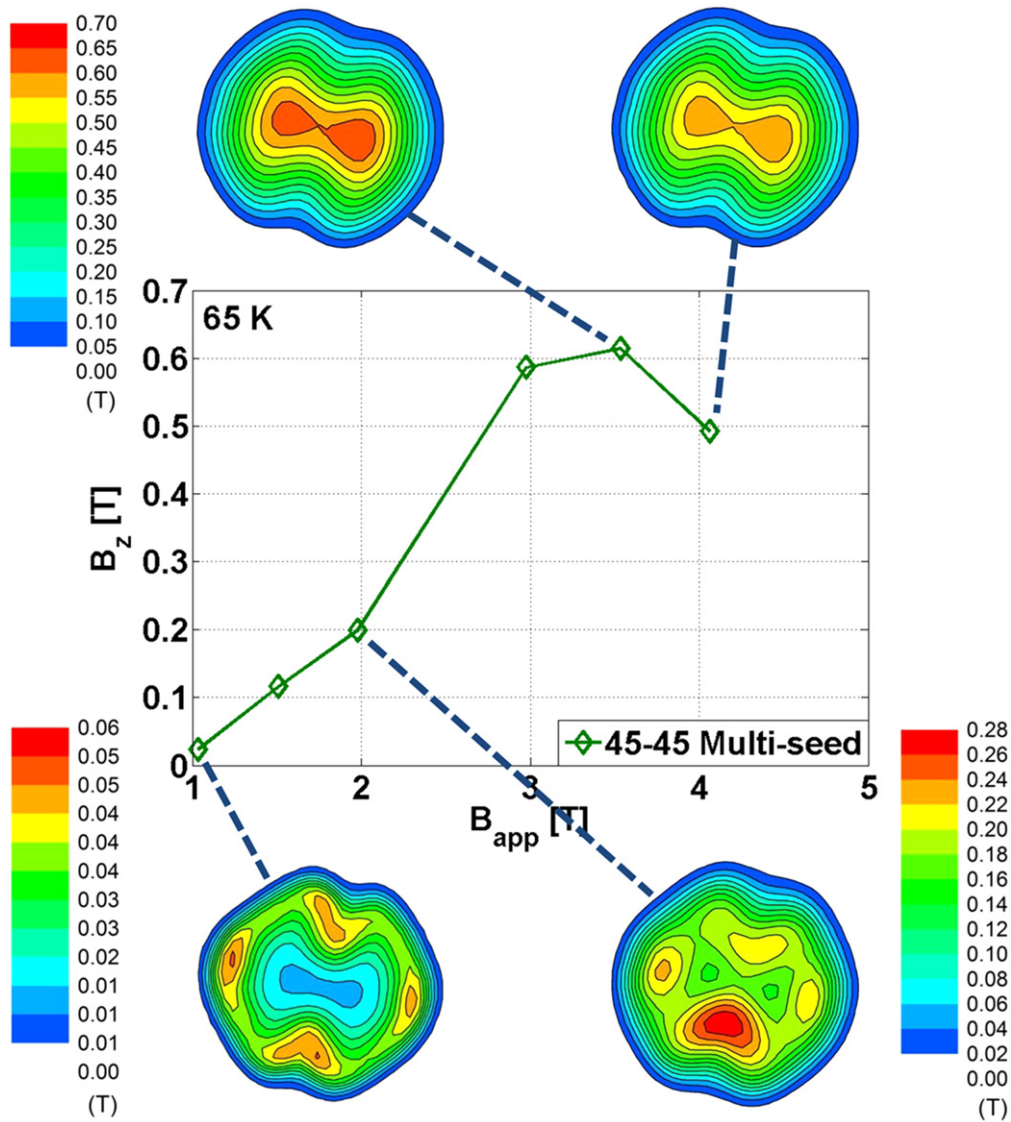
$B_{app} = 6.4$  T with a rise time of  $t_r = 12$  ms and duration of approximately  $t_d = 120$  ms [24].

After PFM of the sample, the two-dimensional trapped field distributions were measured inside the vacuum chamber using an  $x$ – $y$  stage controller and an axial-type Hall sensor positioned above the top surface of the samples. The trapped field close to the centre of the sample were measured dynamically during the application of each pulsed field using the same Hall sensor (located on the top surface of the samples).

**3.2.1. Trapped field performance using PFM.** Figure 5 shows the trapped field for both samples magnetized by PFM at operating temperatures around 40 K and 65 K, measured at the centre of the top bulk surface ( $z = 0$  mm). For the lower operating temperature, the trapped field is almost doubled in

both samples. When the external field exceeds the full activation field (defined as the minimum field required to fully magnetize the bulk sample [24]), and with increasing magnitude of the external applied field, the maximum trapped field decreases, due to an increasing temperature rise from the more rapid movement of flux lines within the sample [24].

Compared with the FC magnetization results (see figures 3 and 4), which indicate a significantly higher trapped field capability for the 45°–45° multi-seed sample, the maximum, central trapped field for PFM appears to be lower than that for the 0°–0° bulk sample and the optimal activation field is slightly higher at both operating temperatures (40 K and 65 K).



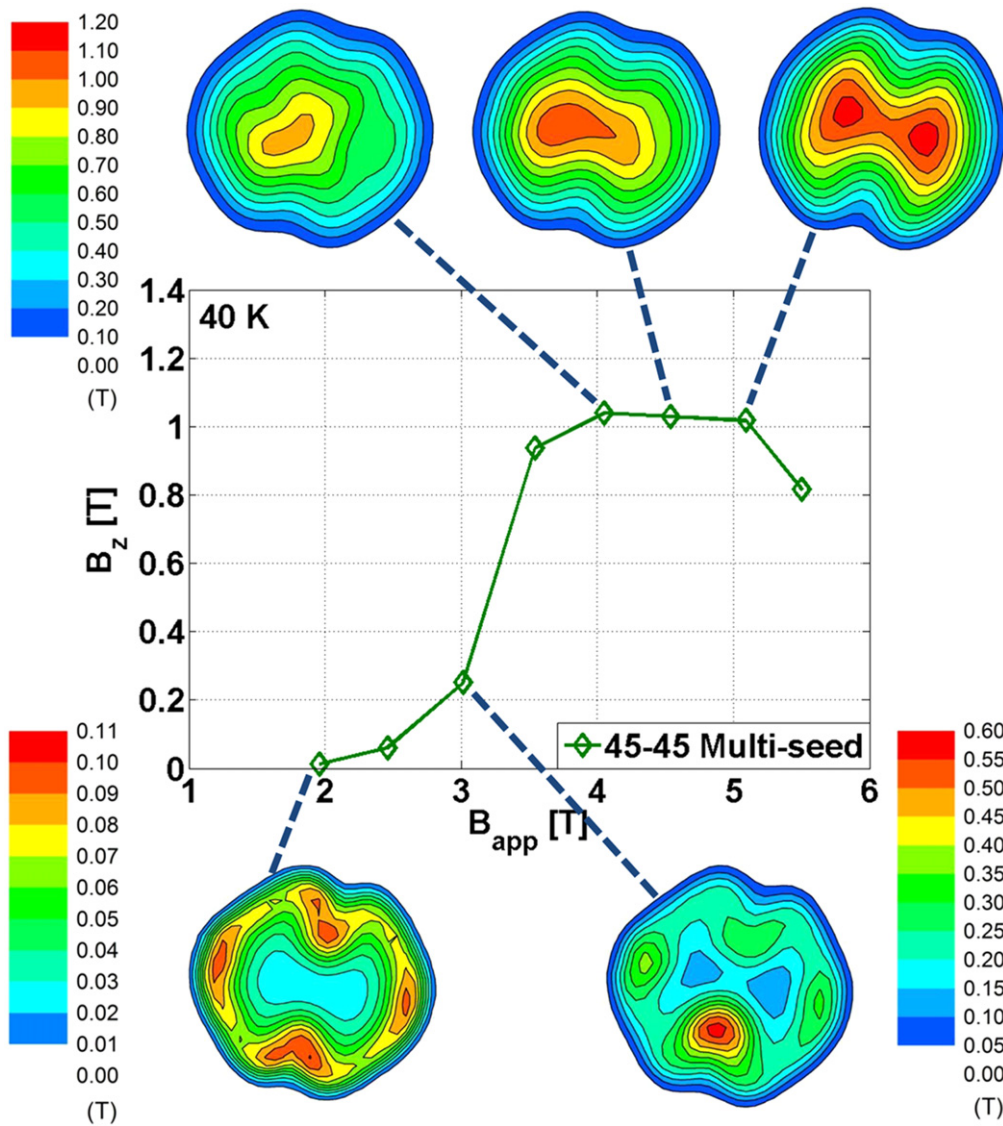
**Figure 7.** 2D trapped field profiles measured on the top surface ( $z = 1$  mm) for the  $45^\circ$ – $45^\circ$  multi-seed sample at 65 K. The central panel shows the corresponding central trapped field, as shown in figure 5. The samples are arranged in the same position as shown in figure 2.

Figure 6 presents the total trapped flux,  $\Phi_T$ , for both samples at 40 and 65 K, measured 1 mm above the bulk surface, as a function of the applied pulsed field,  $B_{app}$ .  $\Phi_T$  is calculated from the 2D trapped field profiles presented in the next section. Although both samples have an almost similar total flux trapping capability when magnetized by PFM, the flux dynamics and trapped field profiles for the two samples are very different, and this behaviour is examined in detail in the following section.

**3.2.2. 2D PFM trapped field profiles.** Figures 7 and 8 show the 2D trapped field profiles for the  $45^\circ$ – $45^\circ$  multi-seed sample at 65 K and 40 K, respectively. The trapped field distribution is distorted due to the inhomogeneous  $J_c$  distribution generated during the growth process, but this is significantly different in comparison with standard YBCO samples [24]. This will be analyzed numerically in detail in

section 4. When the external applied field is lower than the activation field, the trapped field is localized at particular locations around the edge of the bulk sample. However, when fully magnetized, two well-defined peaks appear in the trapped field profile of the sample. For the lower temperature (40 K), the magnitude of the trapped field profile increases, but the dynamics of the flux penetration show a similar trend to those at 65 K.

The 2D trapped field profiles for the  $0^\circ$ – $0^\circ$  multi-seed sample at 65 K and 40 K are shown in figures 9 and 10, respectively. The trapped field profiles here differ from the  $45^\circ$ – $45^\circ$  multi-seed sample due to the different orientation of the seeds, and hence the growth boundaries (as shown in figure 1). There are clearly defined symmetric twin peaks in the trapped field profile for the  $45^\circ$ – $45^\circ$  sample; however, the  $0^\circ$ – $0^\circ$  sample shows an asymmetric trapped field with peaks of different magnitude. Since a well-defined, symmetric trapped field profile is desirable for practical applications, the



**Figure 8.** 2D trapped field profiles measured on the top surface ( $z = 1$  mm) for the  $45^\circ$ – $45^\circ$  multi-seed sample at 40 K. The central panel shows the corresponding central trapped field, as shown in figure 5. The samples are arranged in the same position as shown in figure 2.

$45^\circ$ – $45^\circ$  sample exhibits a better trapped field profile with more potential for practical/commercial applications.

**3.2.3. Dynamics of magnetic flux penetration during PFM ( $45^\circ$ – $45^\circ$  multi-seed sample).** In this section, we analyze the magnetic flux penetration into the  $45^\circ$ – $45^\circ$  multi-seed sample at 65 and 40 K, in order to better understand the flux dynamics and provide guidance for the numerical simulations carried out in section 4. From the trapped field profiles presented in figures 7 and 8, the flux penetrates along the A- and B-lines shown in figure 11: the A-line is along the growth sector boundaries (GSBs) through the two seed positions and the B-line passes across the GSB between the two seeds.

Figure 12 shows the cross-section of the trapped field profile along the A-line (see figure 11) for various applied magnetic fields,  $B_{app}$ , at operating temperatures of around 65 K (top) and 40 K (bottom). When the external magnetic field is relatively small (e.g.,  $B_{app} < 3$  T at 40 K and

$B_{app} < 2$  T at 65 K), resulting in only partial magnetization, the flux is trapped in the regions other than the seed positions with a relatively small  $J_c$ . However, for a larger external pulsed field (close to or higher than the full activation field ( $B_{app} > 4$ – $5$  T at 40 K and  $B_{app} > 3$  T at 65 K)), the flux is trapped in regions of higher  $J_c$  [24]. Therefore, based on figure 12, when  $B_{app} = 3.01$  T at 40 K, the trapped field has a pattern as a ‘high-low-high-low-high’ characteristic, which implies the  $J_c$  at around  $\pm 5$  mm across the seed, where the bridge seed is located, is relatively high. When the applied field increases, flux is trapped around the seed, which also implies that  $J_c$  around seeds is relatively high, compared to  $J_c$  over the bulk surface. In both figures 12 and 13,  $x = 0$  mm corresponds to the same point: the centre of the top surface of the bulk samples.

Figure 13 shows the cross-section of the trapped field profile along the B-line (see figure 11) for various applied magnetic fields,  $B_{app}$ . At  $B_{app} = 3.01$  T at 40 K and 1.98 T at

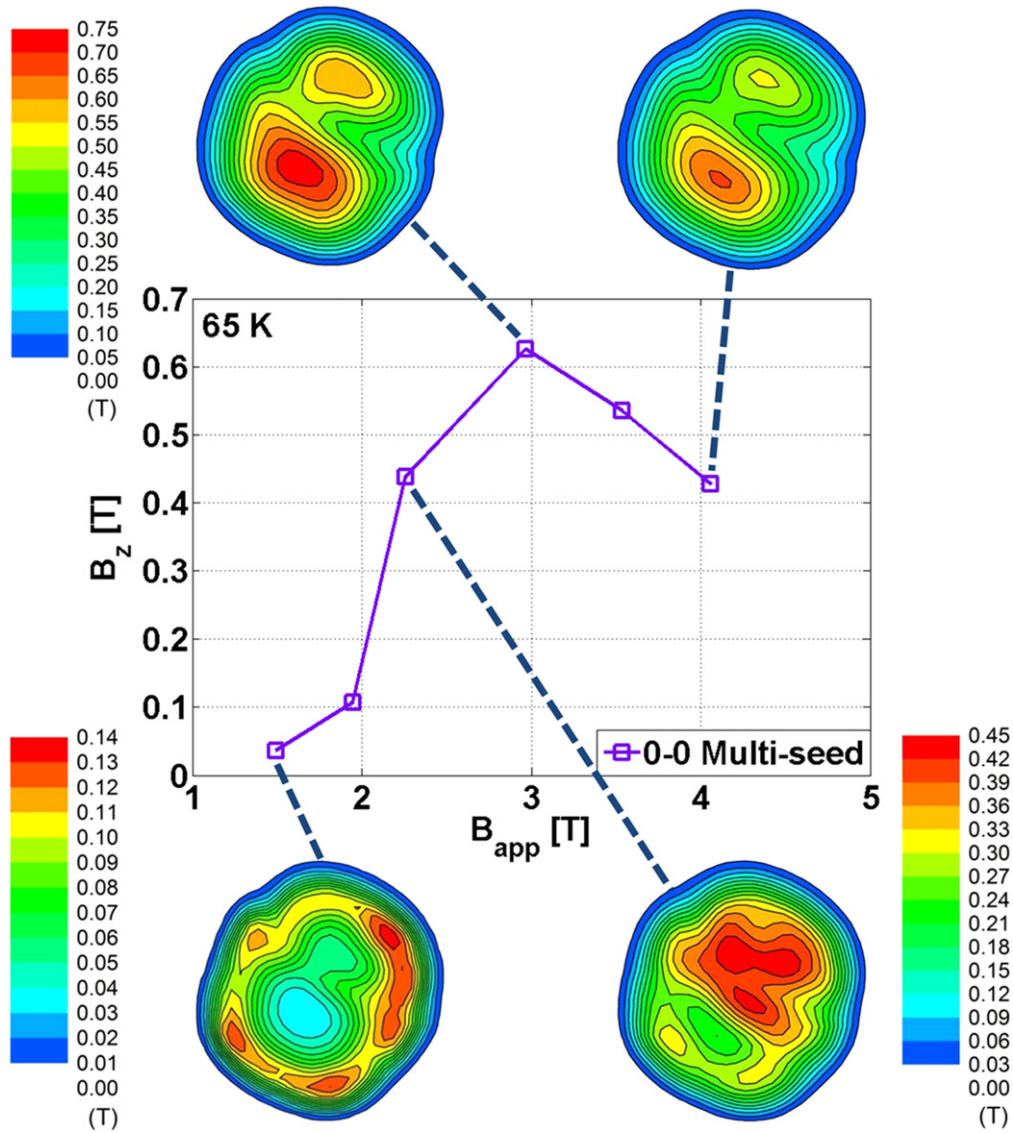


**Figure 9.** 2D trapped field profiles measured on the top surface ( $z = 1$  mm) for the  $0^\circ$ – $0^\circ$  multi-seed sample at 65 K. The central panel shows the corresponding central trapped field, as shown in figure 5. The samples are arranged in the same position as shown in figure 2.

65 K, there is a valley in the trapped field profile in between the seed, which implies that  $J_c$  across the facet line between the seeds is relatively large compared to other regions along the B-line. When the applied field is over the activation field, it exhibits a well-defined peak similar to a traditional trapped field profile.

Therefore,  $J_c$  across the two seeds (along the A-line) is highest around the seeds, and  $J_c$  in between the seeds (along the B-line), along the facet line (GSB) between the two seeds, also has high  $J_c$ , but is slightly lower. These analyzes provide the basis for the assumptions made in the numerical simulation in the next section.

#### 4. Numerical simulation

The alignment of the seeds in the multi-seeding process is critical and the bridge seeds provide the best alignment of the

two seeds in both  $45^\circ$ – $45^\circ$  and  $0^\circ$ – $0^\circ$  oriented samples, which results in the successful fabrication of multi-seed samples with trapped fields that are comparable to those obtained using single seeds. However, as shown in figure 3, the grain boundaries created by using  $45^\circ$ – $45^\circ$  seeds have a less significant effect on the overall trapped field when magnetized by FC. An impurity-free boundary can be engineered between the two seed legs of the bridge when  $45^\circ$ – $45^\circ$  bridge seeds are used to enlarge YBCO single grains [21]. Since in the numerical simulation a more ideal case needs to be considered and we need to deduce the influence of boundary effects in the model, the  $45^\circ$ – $45^\circ$  multi-seed sample at 65 K is used as an example to carry out the numerical analysis in this section.

##### 4.1. Modelling framework

Here, the trapped field performance of a  $45^\circ$ – $45^\circ$  bridge-seeded multi-seed sample is investigated qualitatively using a

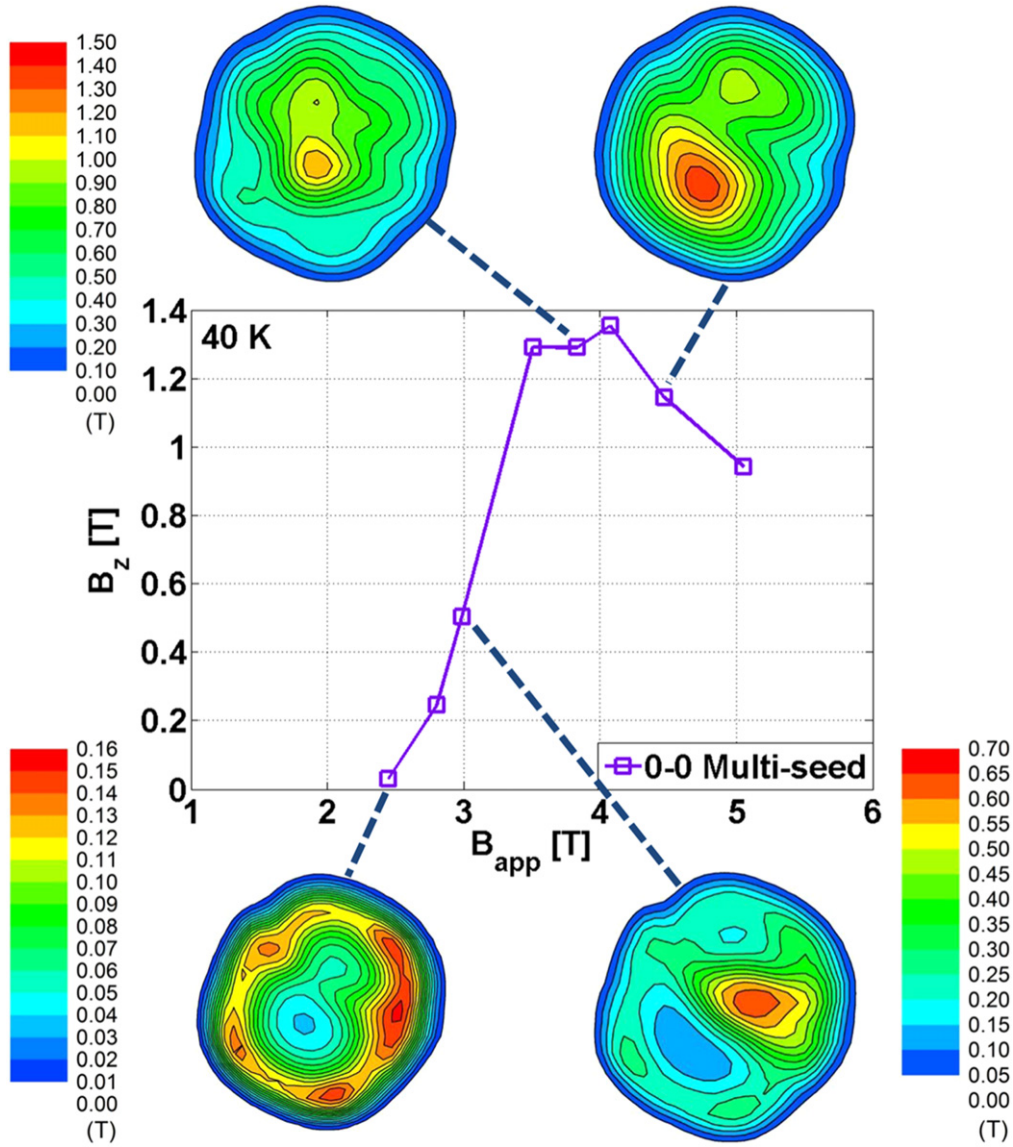


**Figure 10.** 2D trapped field profiles measured on the top surface ( $z = 1$  mm) for the  $0^\circ$ - $0^\circ$  multi-seed sample at 40 K. The central panel shows the corresponding central trapped field, as shown in figure 5. The samples are arranged in the same position as shown in figure 2.

3D finite-element model. This model is based on the  $\mathbf{H}$ -formulation [25–31], which has been employed previously by the authors to investigate the trapped field performance and characteristics of bulk superconductors [24, 32–34], and is implemented using COMSOL Multiphysics 4.3a [35].

In the model, the governing equations are based on Maxwell's equations (Faraday's and Ampere's laws), shown as (2) and (3), respectively:

$$\nabla \times \mathbf{E} = -\frac{\partial \mathbf{B}}{\partial t} = -\mu_0 \frac{\partial \mathbf{H}}{\partial t}, \quad (2)$$

$$\nabla \times \mathbf{H} = \mathbf{J}. \quad (3)$$

The electrical properties of the superconductor are modelled using an  $E$ - $J$  power law relation [36, 37],  $E \propto J^n$ , where  $n = 21$ . An external pulsed magnetic field is applied to the bulk along the  $c$ -axis of sample, perpendicular to the top surface, by setting appropriate boundary conditions [24]. This

3D model is based on the model framework presented in [24], but the assumptions regarding  $J_c$  must be changed appropriately to account for the particular  $J_c$  distribution of the multi-seed samples, which differs from that presented in [24] for a standard YBCO sample. In order to simplify the situation, the field dependence of  $J_c$  is not considered here.

Based on the analysis in section 3.2.3,  $J_c$  varies around the  $ab$ -plane of the multi-seed sample, where  $J_c$  is slightly higher along the facet lines (assumed as  $1.2 \times J_{c0}$ , where  $J_{c0} = 3.2 \times 10^8 \text{ A m}^{-2}$  at 65 K) and the lowest  $J_c$  is around the edge of the sample (assumed as  $0.4 \times J_{c0}$ ), with  $J_c$  varying as a cosine function, as shown as in figure 14.  $J_c$  along the  $c$ -axis (i.e., along the thickness of the sample) is considered to have the same  $J_c$  distribution. This varying  $J_c$  distribution around the  $ab$ -plane can be described using a set of mathematical functions and a polar coordinate system as described below.

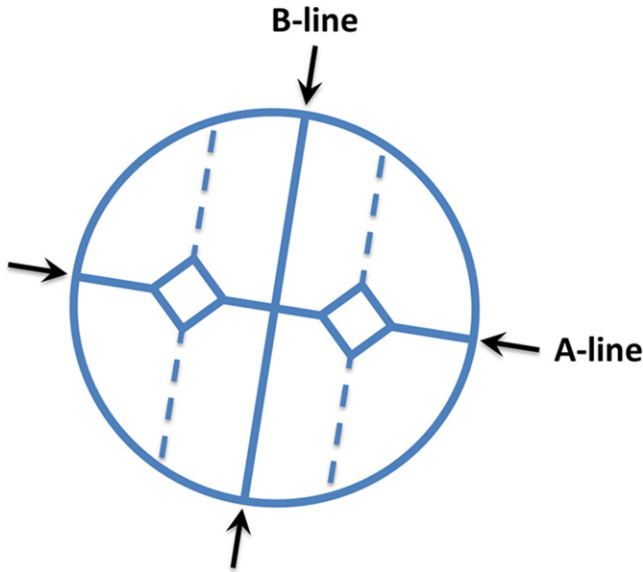


**Figure 11.** Schematic illustration of flux penetration analysis for the 45°–45° multi-seed sample: the A-line is along the GSBs through the two seed positions and the B-line passes across the GSB between the two seeds.

In figure 14, region 1 represents the relatively higher  $J_c$  around the seeds and facet lines/GSBs of the multi-seed sample. Region 4 exhibits the lowest  $J_c$ , and regions 2 and 3 represent a gradually decreasing  $J_c$  between the GSB towards the growth sector region (GSR). The mathematical equations describing  $J_c$  for each region are as follows, where the angle  $\theta$  is defined anti-clockwise from the horizontal dashed line dividing region 4 and regions 1, 2 and 3:

**Region 1** ( $45^\circ \leq \theta \leq 135^\circ$ ):

$$J_c = J_{c0}(1 + 0.2 \times \cos(4\theta)). \quad (4)$$

**Regions 2** ( $135^\circ \leq \theta \leq 180^\circ$ ) **and 3** ( $0^\circ \leq \theta \leq 45^\circ$ ):

$$J_c = 0.4J_{c0}(1 - \cos(2\theta)) + 0.4J_{c0}. \quad (5)$$

**Region 4** ( $0^\circ \geq \theta \geq -180^\circ$ ):

$$J_c = 0.4J_{c0}. \quad (6)$$

Equation (4) describes the variation of  $J_c$  in region 1, with a maximum  $1.2J_{c0}$  close to the GSBs and  $0.8J_{c0}$  around the GSRs. Equation (5) describes the  $J_c$  distribution in regions 2 and 3, varying from  $0.8J_{c0}$  to  $0.4J_{c0}$ , and region 4 is governed by equation (6).

Since the temperature of bulk superconductors can change significantly during PFM [9], the electromagnetic model is coupled with a thermal model in this simulation, which is extended from our previous models [24, 33]. A thermally-isolated model of a bulk superconductor is used to simulate the bulk sample being submersed in sub-cooled liquid nitrogen at 65 K, with the specific heat and thermal conductivity along the *ab*- and *c*-planes assumed as  $C = 164.25 \text{ J/(kg K)}$ ,  $\kappa_{ab} = 15.49 \text{ W/(m K)}$ , and  $\kappa_c = 3.63 \text{ W/(m K)}$ , respectively. The thermal behaviour, from equation (7), is coupled to the

electromagnetic model using equations (8) and (9):

$$\rho \cdot C \frac{dT}{dt} = \nabla \cdot (k \nabla T) + Q. \quad (7)$$

The temperature dependence of  $J_{c0}(T)$  is given by:

$$J_{c0}(T) = \alpha \left[ 1 - \left( \frac{T}{T_c} \right)^2 \right]^{1.5}, \quad (8)$$

where  $\alpha = 9.1 \times 10^8 \text{ A m}^{-2}$  is the critical current density extrapolated to  $T = 0 \text{ K}$ . The heat source,  $Q$ , in the thermal model is calculated from the product of the electric field and current density throughout the sample, defined as

$$Q = E \cdot J, \quad (9)$$

where  $E = \sqrt{E_x^2 + E_y^2 + E_z^2}$  and  $J = \sqrt{J_x^2 + J_y^2 + J_z^2}$ .

#### 4.2. Comparison of experimental and numerical simulation results

The trapped field profiles as simulated numerically are compared with the experimental results for external applied fields of 1, 2, 3 and 4 T, as shown in figures 15–18. These figures show that the simulation results agree qualitatively well with the experimental data. When the external field is much smaller than the activation field, the field required to fully magnetize the bulk sample, the flux only penetrates and stays within regions with relatively lower  $J_c$  (see figures 15 and 16). However, when the applied pulse is above the activation field (approximately 3 T in this case), there are two peaks in the trapped field profile (figure 17), and when  $B_{app}$  is much larger than the activation field, the trapped field decreases overall, but still presents two peaks (see figure 18). The shape of the trapped field distribution from PFM is determined by the length of bridge seed and the boundary generated during the growth process. These results also agree with the experimental data presented previously in [19–21].

#### 4.3. Influence of bridge seed length

In this section, the influence of the length of the bridge seed is investigated using the same numerical model. The length of the bridge seed,  $L$ , is varied between 2 and 12 mm and it is observed in figure 19(a) that with increasing distance between the two seeds, the maximum trapped field of any peak decreases, as does the trapped field at the centre of the bulk. Another important measure of the performance of bulk superconductor samples is the total trapped flux,  $\Phi_T$ , in the sample and figure 19(b) shows  $\Phi_T$  increases as the length of the bridge seed increases, although the peak trapped field decreases. Finally, figure 20 shows the trapped field distribution across the top surface of the bulk for lengths of 2, 4, 8 and 12 mm. When the bridge length is short, e.g., 2 mm, there is only one peak observed in the trapped field distribution. However, as the bridge length is increased, a two-peak pattern begins to emerge and is clearly observed for the longest bridge lengths. It should be noted that the slight asymmetry in the trapped field distribution is an artefact of the fine, but finite, mesh discretization used. These simulation

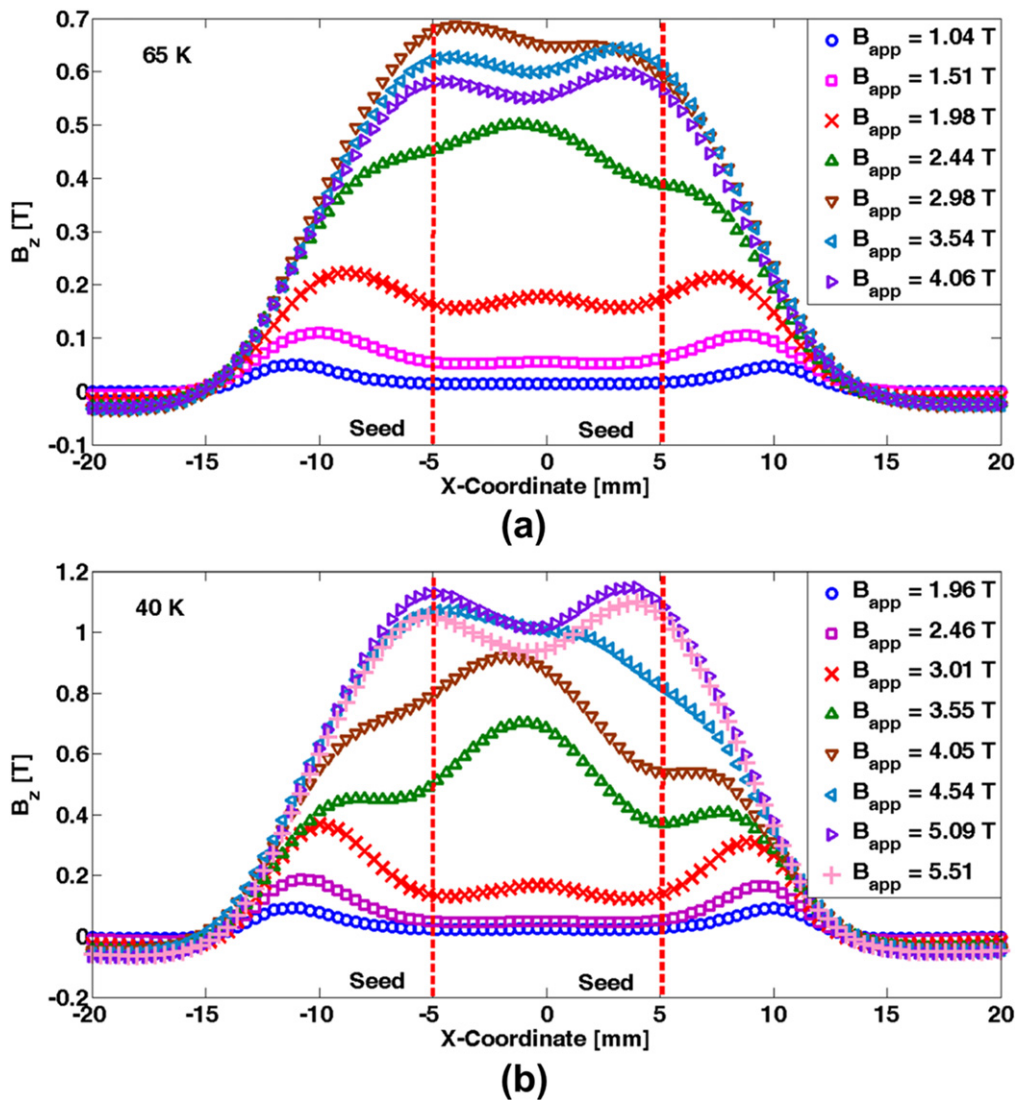


**Figure 12.** Flux penetration profiles for the  $45^{\circ}$ – $45^{\circ}$  multi-seed sample across the seeds (from the left and right, along the A-line, as shown in figure 11) at operating temperatures of around (a) 65 K and (b) 40 K.

results agree qualitatively well with the experimental results presented in [19] and this kind of 3D modelling framework can provide useful guidance for the processing of multi-seed samples to optimize their performance for a particular application.

## 5. Conclusion

The multi-seeding process has the potential to enlarge the sample size of bulk (RE)BCO superconductors with improved fabrication speed in order to deliver large, single grains for practical applications and the so-called bridge-seeding produces the best alignment of two seeds when melt-processing such samples. In this paper, two multi-seed samples—one with a  $45^{\circ}$ – $45^{\circ}$  and another with a  $0^{\circ}$ – $0^{\circ}$  bridge seed—were magnetized by PFM at temperatures of 65 and 40 K and the trapped field performance and magnetic flux dynamics were studied.

The samples were firstly magnetized using the FC magnetization technique, which gives the best indication of the trapped field capability of a bulk superconductor sample. Although the FC results indicated a significantly higher trapped field capability for the  $45^{\circ}$ – $45^{\circ}$  multi-seed sample, the maximum, central trapped field for PFM was lower than that for the  $0^{\circ}$ – $0^{\circ}$  bulk sample and the total flux trapping capability when magnetized by PFM was almost the same at both temperatures. However, the flux dynamics during the PFM process for the two samples are very different, which were investigated using 2D trapped field profiles measured across the top surface of each sample.

By analyzing the flux penetration into the better-performing  $45^{\circ}$ – $45^{\circ}$  multi-seed sample, an estimated  $J_c$  distribution over the  $ab$ -plane was determined, and this was input into a 3D finite-element model, which was then used to qualitatively reproduce the experimental results to good effect. This numerical model was then used to investigate the influence of the length of the bridge seed on the trapped field distribution

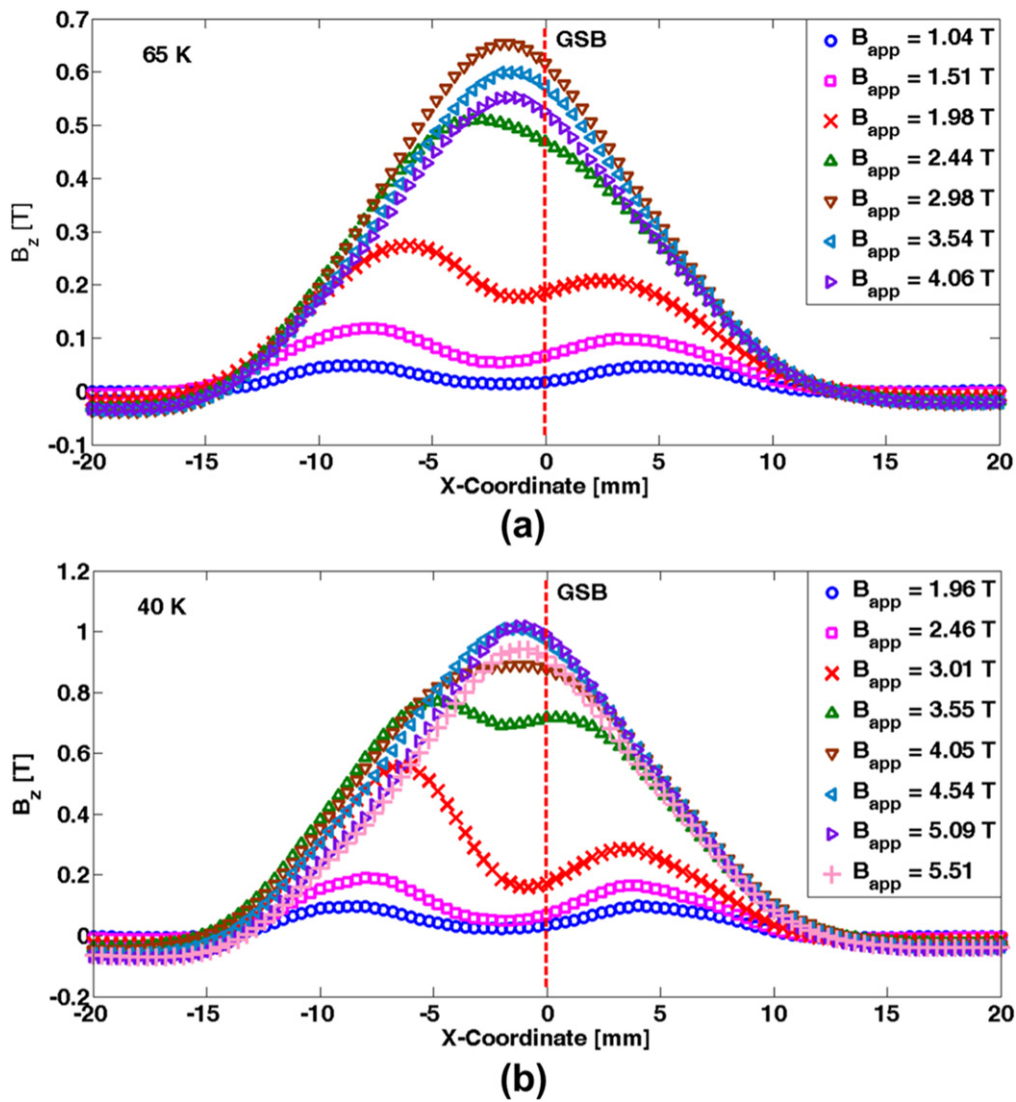


**Figure 13.** Flux penetration profiles for the 45°–45° multi-seed sample in between the seeds (from the top and bottom, along the B-line, as shown in figure 11) at operating temperatures of around (a) 65 K and (b) 40 K.

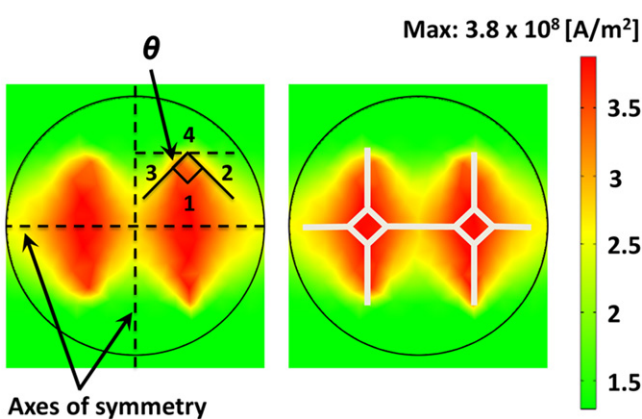


**Figure 14.** Schematic illustration of the mathematical function and polar coordinate system (left) and the  $J_c$  distribution across the  $ab$ -plane (right). The  $J_c$  distribution includes the locations of the seeds and the GSBs, shown by the solid white lines.

and total trapped flux. For increasing bridge length, the trapped field distribution shows a clear two-peak pattern and there is a reduction in the peak and central magnetic flux densities. However, the total trapped flux is increased with increasing bridge length. This modelling framework will provide useful guidance for the processing of such multi-seed samples in the future in order to optimize their performance.

**Acknowledgments**

Mark Ainslie would like to acknowledge the support of a Royal Academy of Engineering Research Fellowship. Jin Zou would like to acknowledge the support of Churchill College, Cambridge, the China Scholarship Council and the Cambridge Commonwealth, European and International Trust. Hiroyuki Fujishiro would like to acknowledge support in part

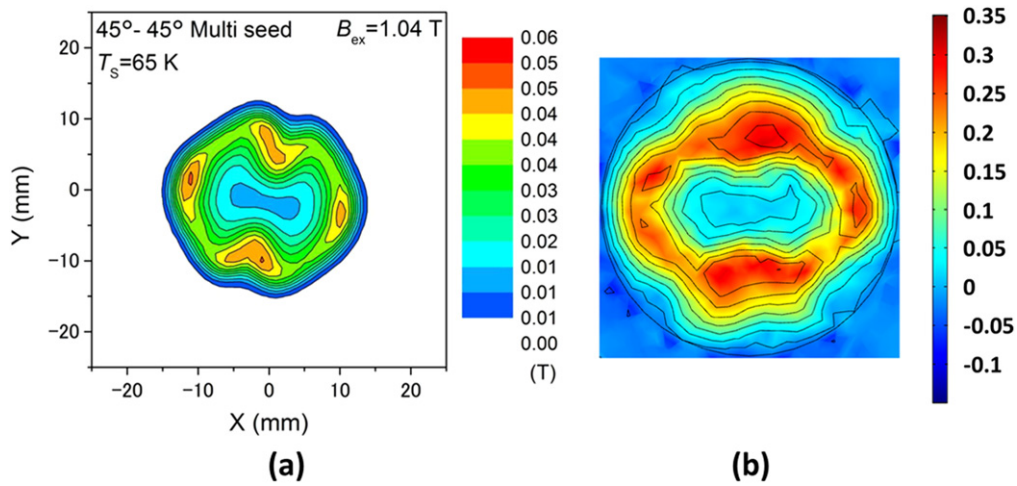


**Figure 15.** Comparison of (a) experimental and (b) numerical simulation results for the PFM trapped field profile at 1 mm above the 45°–45° multi-seed sample when  $B_{app} = 1$  T.

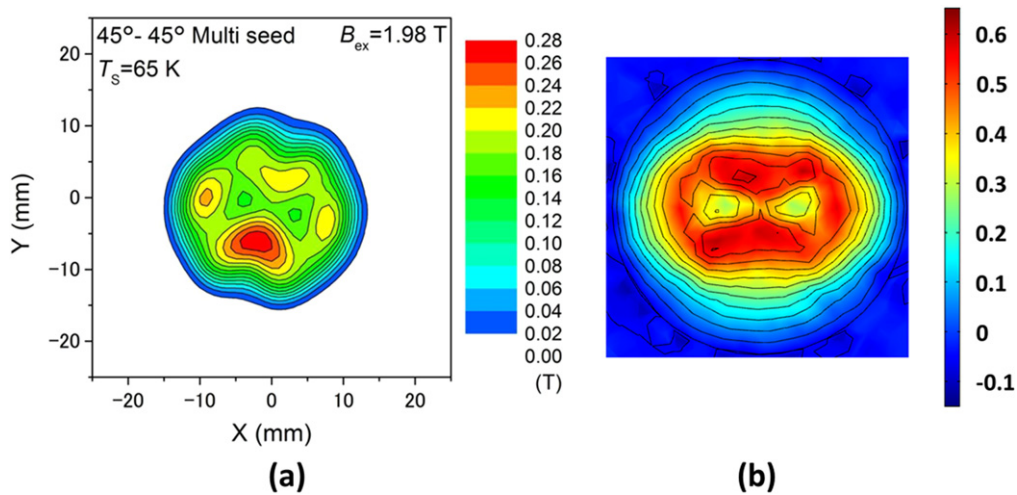


**Figure 16.** Comparison of (a) experimental and (b) numerical simulation results for the PFM trapped field profile at 1 mm above the 45°–45° multi-seed sample when  $B_{app} = 2$  T.

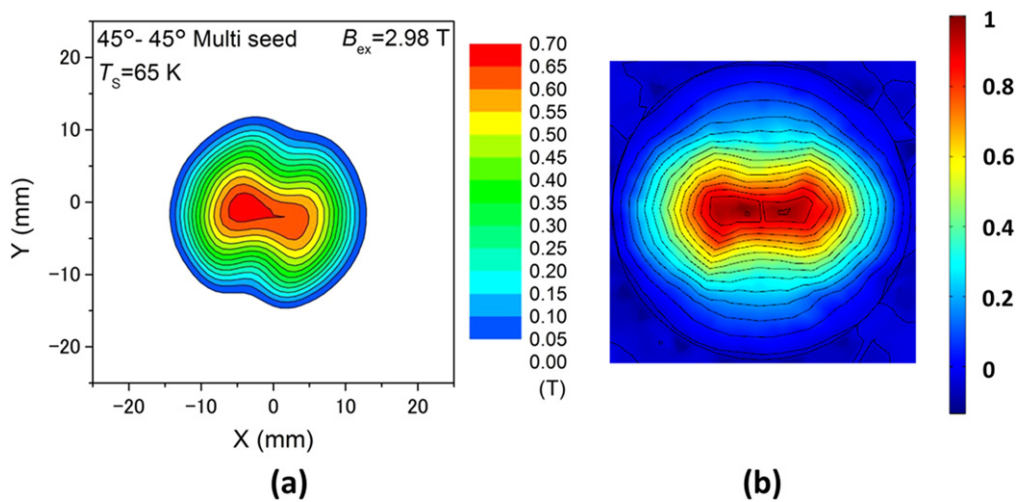


**Figure 17.** Comparison of (a) experimental and (b) numerical simulation results for the PFM trapped field profile at 1 mm above the 45°–45° multi-seed sample when  $B_{app} = 3$  T.

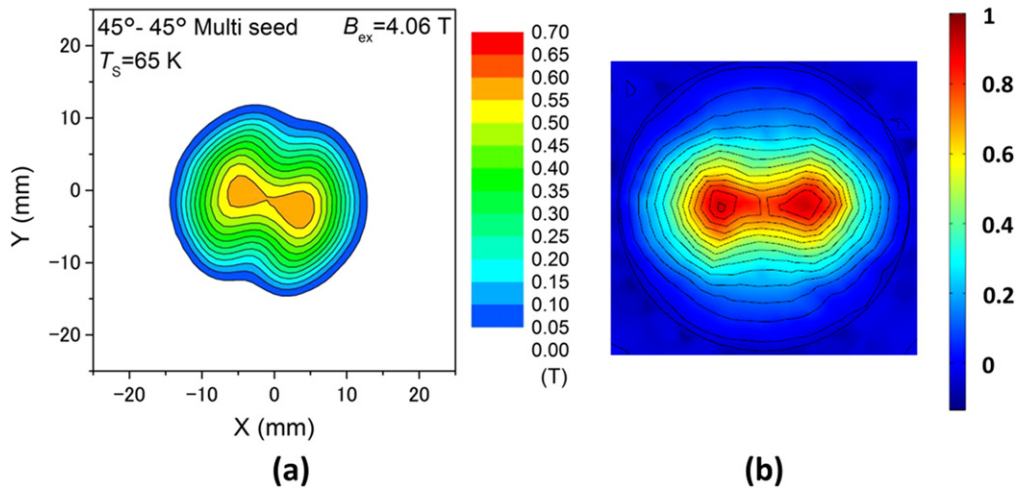


**Figure 18.** Comparison of (a) experimental and (b) numerical simulation results for the PFM trapped field profile at 1 mm above the 45°–45° multi-seed sample when  $B_{app} = 4$  T.

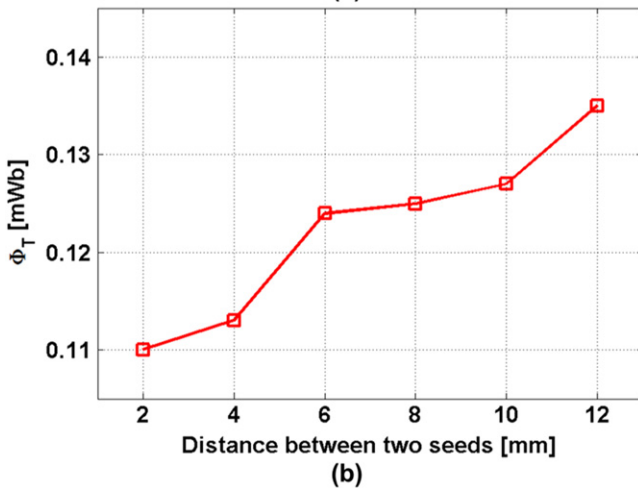
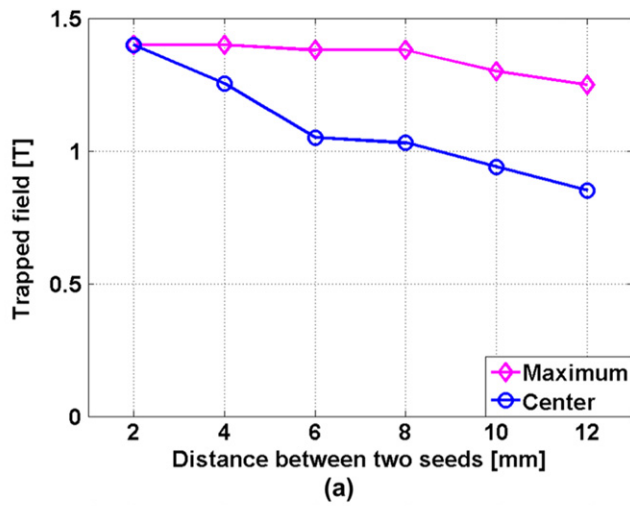


**Figure 19.** Numerical simulation results when the bridge seed length ( $L$ ) is varied between 2 and 12 mm, for an applied pulsed field equal to the full activation field of each bulk sample: (a) maximum trapped field of any peak and trapped field at the centre of the sample, (b) total trapped flux,  $\Phi_T$ .

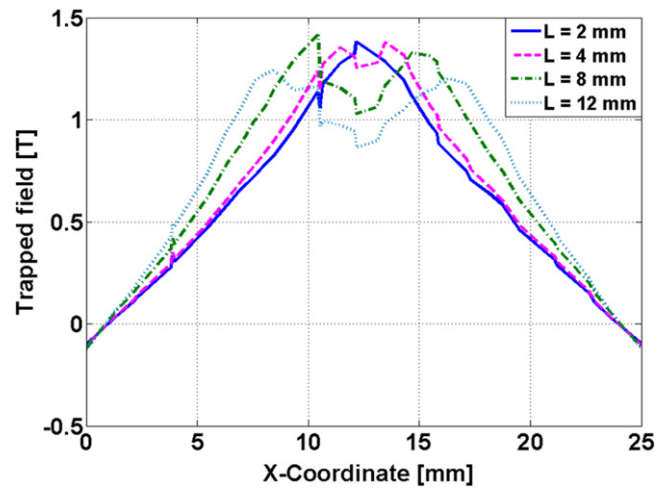


**Figure 20.** Numerical simulation results showing the trapped field distribution across the top surface of each bulk sample for bridge seed lengths of 2, 4, 8 and 12 mm. The centre of the bulk corresponds to  $x = 12.5$  mm.

by a Grant-in-Aid for Scientific Research from the Ministry of Education, Culture, Sports, Science and Technology, Japan. This research was also supported in part by a Royal Society International Exchanges Scheme grant, IE131084.

**References**

- [1] Tomita M and Murakami M 2003 *Nature* **421** 517–20
- [2] Durrell J H *et al* 2014 *Supercond. Sci. Technol.* **27** 082001
- [3] Nariki S, Sakai N and Murakami M 2005 *Supercond. Sci. Technol.* **18** S126–30
- [4] Zhou D *et al* 2012 *Supercond. Sci. Technol.* **25** 103001
- [5] Hull J R 2000 *Supercond. Sci. Technol.* **13** R1–15
- [6] Sino H, Nagashima K and Arai Y 2008 *J. Phys.: Conf. Ser.* **97** 012101

- [7] Koshizuka N 2006 *Physica C* **445–8** 1103
- [8] Oka T 2007 *Physica C* **463–5** 7
- [9] Bean C P 1962 *Phys. Rev. Lett.* **8** 250
- [10] Bean C P 1962 *Rev. Mod. Phys.* **36** 31
- [11] Ainslie M D and Fujishiro H 2015 *Supercond. Sci. Technol.* **28** 053002
- [12] Kim C-J, Hong G-W and Oh H-J 2001 *Physica C* **357–60** 635
- [13] Kim C-J *et al* 2000 *Physica C* **338** 205
- [14] Kim C-J *et al* 2000 *Physica C* **336** 233
- [15] Haindl S *et al* 2005 *IEEE Trans. Appl. Supercond.* **15** 3129
- [16] Wongsatanawarid A, Seki H and Murakami M 2010 *J. Phys.: Conf. Ser.* **234** 012047
- [17] Li T *et al* 2010 *J. Appl. Phys.* **108** 023914
- [18] Todt V *et al* 1996 *Appl. Phys. Lett.* **69** 3746
- [19] Shi Y-H, Durrell J H, Dennis A R and Cardwell D A 2013 *Supercond. Sci. Technol.* **26** 015012
- [20] Shi Y-H *et al* 2012 *Supercond. Sci. Technol.* **25** 045006
- [21] Shi Y-H *et al* 2013 *J. Am. Ceram. Soc.* **96** 1757–62
- [22] Shi Y-H, Babu Hari N and Cardwell D A 2005 *Supercond. Sci. Technol.* **18** L13–6
- [23] Babu Hari N, Shi Y-H, Iida K and Cardwell D A 2005 *Nat. Mater.* **4** 476–80
- [24] Ainslie M D *et al* 2014 *Supercond. Sci. Technol.* **27** 065008
- [25] Hong Z, Campbell A M and Coombs T A 2006 *Supercond. Sci. Technol.* **19** 1246
- [26] Ainslie M D, Flack T J, Hong Z and Coombs T A 2011 *Int. J. Comput. Math. Electr. Electron. Eng.* **30** 762
- [27] Ainslie M D, Flack T J and Campbell A M 2012 *Physica C* **472** 50
- [28] Ainslie M D *et al* 2011 *Supercond. Sci. Technol.* **24** 045005
- [29] Zhang M and Coombs T A 2012 *Supercond. Sci. Technol.* **25** 015009
- [30] Ainslie M D, Yuan W and Flack T J 2013 *IEEE Trans. Appl. Supercond.* **23** 4700104
- [31] Zermeno V, Grilli F and Sirois F 2013 *Supercond. Sci. Technol.* **26** 052001
- [32] Zou J *et al* 2015 *IEEE Trans. Appl. Supercond.* **25** 4900505
- [33] Zou J *et al* 2015 *Supercond. Sci. Technol.* **28** 035016
- [34] Zou J *et al* 2015 *Supercond. Sci. Technol.* **28** 075009
- [35] COMSOL, Inc. ([www.comsol.com](http://www.comsol.com))
- [36] Plummer C J G and Evetts J E 1987 *IEEE Trans. Magn.* **23** 1179–82
- [37] Rhyner J 1993 *Physica C* **212** 292–300